Author(s): Sayab, Mohammad; Miettinen, Arttu; Aerden, Domingo; Karell, Fredrik

Title: Orthogonal switching of AMS axes during type-2 fold interference : Insights from integrated X-ray computed tomography, AMS and 3D petrography

Year: 2017

Version:

Please cite the original version:

Sayab, M., Miettinen, A., Aerden, D., & Karell, F. (2017). Orthogonal switching of AMS axes during type-2 fold interference : Insights from integrated X-ray computed tomography, AMS and 3D petrography. Journal of Structural Geology, 103, 1-16. https://doi.org/10.1016/j.jsg.2017.09.002

Orthogonal switching of AMS axes during type-2 fold interference: Insights from integrated X-ray computed tomography, AMS and 3D petrography

Mohammad Sayab, Arttu Miettinen, Domingo Aerden, Fredrik Karell

PII: S0191-8141(17)30173-6

DOI: 10.1016/j.jsg.2017.09.002

Reference: SG 3520

To appear in: *Journal of Structural Geology*

Received Date: 7 June 2017

Revised Date: 23 August 2017

Accepted Date: 1 September 2017

Orthogonal switching of AMS axes during type-2 fold interference: Insights from integrated X-ray computed tomography, AMS and 3D petrography

Mohammad Sayab[1*], Arttu Miettinen[2], Domingo Aerden[3], Fredrik Karell[1]
[1]Geological Survey of Finland, P.O. Box 96, FI-02151 Espoo, Finland
[2]Department of Physics, University of Jyvaskyla P.O. Box 35, FI-40014, Finland
[3]Departamento de Geodinámica and IACT-CSIC, Universidad de Granada, Granada 18002, Spain
*Corresponding author: sayab.muhammad@gtk.fi

Abstract

We applied X-ray computed microtomography (μ-CT) in combination with anisotropy of magnetic susceptibility (AMS) analysis to study metamorphic rock fabrics in an oriented drill core sample of pyrite-pyrrhotite-quartz-mica schist. The sample is extracted from the Paleoproterozoic Martimo metasedimentary belt of northern Finland. The μ-CT resolves the spatial distribution, shape and orientation of 25,920 pyrrhotite and 153 pyrite grains localized in mm-thick metapelitic laminae. Together with microstructural analysis, the μ-CT allows us to interpret the prolate symmetry of the AMS ellipsoid and its relationship to the deformation history. AMS of the sample is controlled by pyrrhotite porphyroblasts that grew syntectonically during D1 in subhorizontal microlithons. The short and intermediate axes (K3 and K2) of the AMS ellipsoid interchanged positions during a subsequent deformation (D2) that intensely crenulated S1 and deformed pyrrhotite, while the long axes (K1) maintained a constant position parallel to the maximum stretching direction. However, it is likely that all the three AMS axes switched, similar to the three principal axes of the shape ellipsoid of pyrite porphyroblasts from D1 to D2. The superposition of D1 and D2 produced a type-2 fold interference pattern.

Keywords: microtomography; AMS; microtectonics; magnetic fabric; pyrrhotite; strain

1. Introduction

X-ray computed micro-tomography (μ-CT) is increasingly being applied in structural geology and ore petrology due to its ability to resolve the three-dimensional (3D) shape and spatial distribution of minerals and associated textures in metamorphic rocks (e.g., Sayab et al., 2015; Macente et al., 2017). Sulfides and oxides yield brighter gray values than rock-forming silicates owing to high X-ray attenuation or higher density. They can be segmented or separated, for example, using the threshold limits of the gray level histogram, and rendered and quantified in 3D volume (e.g., Sayab et al., 2016a; Hanna and Ketcham, 2017). The resulting 3D views provide a spatial distribution of high-density ore minerals (ranging from ca. 4 to 22 g/cm^3) inside a given rock specimen, which is otherwise difficult to determine using serial thin sectioning methods (Hayward, 1990; Aerden, 2003; Bell and Bruce, 2006). The µ-CT technique is non-destructive and can be integrated with a number of conventional and unconventional microstructural methods to investigate regions of interest in extraordinary detail without destroying the whole sample (Kyle and Ketcham, 2015). As a holistic 3D visualization method of analyzing rock fabrics (Sayab et al., 2015), µ-CT is ideal for integrating with measurements of bulk rock anisotropy of magnetic susceptibility (AMS).

AMS measures the directional variations of magnetic susceptibility (K) present in a rock sample, and the AMS magnitude ellipsoid defines the bulk rock orthogonal principal susceptibility axes (K1: maximum, K2: intermediate, K3: minimum; Tarling and Hrouda, 1993). These axes can be correlated with the finite strain axes ($X \geq Y \geq Z$) and structural features, for example mineral stretching and intersection lineations, and, therefore, provide a mean to study deformation in 3D (e.g., Borradaile, 1988; Riller et al., 1996; Ferré et al., 2014; Parsons et al., 2016). However, since AMS measures the sum of different magnetic carrier minerals in a sample, its interpretation requires knowledge of amounts and relative abundances of these minerals, their magnetic susceptibilities, shape preferred orientation (SPO), lattice preferred orientation (LPO) and relationship with tectonic fabrics (e.g., Kruckenberg et al., 2010; Borradaile and Jackson, 2010). Thus, a good understanding of the internal microstructure behind AMS measurements is crucial. High-resolution µ-CT can fulfill this requirement by allowing 3D visualization and determination of statistically volumetric abundances of magnetic carrier minerals and their SPOs. We have explored this possible nexus using an oriented drill core of a pyrrhotite rich micaschist sample that preserves two tectonic foliations. Apart from applying AMS and µ-CT techniques, we studied the sample in three perpendicular thin sections oriented with reference to the matrix foliation. Through this integrated approach, the deformation history of the sample is reconstructed and considered in the regional tectonic framework as revealed by high-fidelity aeromagnetic image (Fig. 1a). The application of non-invasive (AMS and µ-CT) followed by invasive (thin sections) methods illustrated herein offers a means of determining the magnetic lineation and foliation in ore-bearing rocks, which is highly relevant to the exploration of structurally controlled mineral deposits as will be briefly discussed.

2. Tectonic setting and sample description

The Martimo metasedimentary belt forms a part of the Peräpohja region, which lies in the center of the Fennoscandian shield. The area is characterized by lack of topography, where structural field relations in the 3rd dimension are difficult to reconstruct. Five incremental, but heterogeneously distributed deformation events have been proposed for the Martimo belt in a timeframe ranging from 1.92 to 1.77 Ga (Lahtinen et al., 2015). The belt hosts metapelites interbedded with metapsammites and preserves a sequence of near-orthogonal tectonic fabrics that are not fully developed elsewhere in the region (Lahtinen et al., 2015). In particular, the area is passing through a period of extensive geological research because of the recent discoveries of Rompas Au-U and Rajapalot Au (e.g., Nykänen et al., 2017; Ranta et al., 2015; Ranta et al., 2016). Metamorphism in the area is characterized by upper greenschist facies, however, the grade varies from low greenschist facies rocks in the southwest to kyanite bearing migmatites in the northeast (Hölttä and Heilimo, 2017).

An oriented sample (sample 57; Fig. 1; 66° 16' 53.43" N, 24° 29' 24.69" E) was drilled from the middle of the Martimo belt. The drill core sample is characterized by two near-orthogonal foliations that correspond to the D1 and D2 deformations of Lahtinen et al. (2015). S1 is subparallel to S0 (S0//S1) and on average strikes N-S. It is folded with E-W striking axial planes and gently east plunging axes, and overprinted by a steeply dipping, finely-spaced S2 foliation (Fig. 1b). The drill-core sample consists of pyrrhotite-pyrite-quartz mica schist with two distinct foliations (S1 and S2), and thus ideal for integrated µ-CT and AMS studies. Before extracting it from the bedrock using a portable mini-drill, the sample was marked with a north pointing groove on the top surface so that it could be reoriented in the lab. The sample has a 2.5 cm diameter and is 8 cm long.

3. X-ray computed micro-tomography (µ-CT)

3.1. Scanning configuration and processing

The sample was scanned using the high-resolution Phoenix|X-ray Nanotom 180 (GE) scanner at the University of Helsinki. Before scanning the drill core, two brass pins were attached, about 40° from north counting towards the east for reference. The tungsten target X-ray tube was operated with an acceleration voltage of 140 kV and tube current 175 µA. The radiation was filtered with 1.0 mm of Cu. Six hundred views per 360° were acquired, with 1.75 s total exposure time per view. The virtual 3D volume is composed of 1152 horizontal slices with a voxel size of 33 µm × 33 µm × 33 µm. The projections were captured with a Hamamatsu flat panel sensor C7942SK-05. The 3D reconstructions were computed with datos|x – reconstruction software provided by Phoenix|X-ray.

3.2. 3D visualization

After reconstructing the 3D distribution of X-ray attenuations, the contrasting gray shades of pyrrhotite and pyrite allowed us to semi-automatically separate them from the rest of the silicate matrix by mapping gray levels to specific colors using Avizo software (http://www.fei.com/software /avizo -3d -for -materials-science/). Volume rendering further allowed to visualize the dataset in 3D (Figs. 2 and 3). Besides looking at the microtextures in 3D in all directions, it is possible to digitally cut the sample at any angle and to make certain surfaces transparent while rendering others opaque for better visual analysis. A virtual 3D tour inside the sample, at 33 µm voxel resolution, allowed us to closely examine petrographic details and the spatial distribution of sulfides.

To show the penetrative nature and spatial distribution of pyrrhotite and pyrite grains, the drill core was virtually chopped at different horizontal (Fig. 2) and vertical (Fig. 3) levels. The 3D images clearly show that pyrrhotite is present throughout the core but localized within millimeter-scale metasedimentary laminae or bands (S0). Pyrite porphyroblasts are mainly localized along layers in the center (Figs. 3c,e). For better visualization from the top, two such layers were isolated and rendered in red and blue (Fig. 3g). The fold shape, defined by these layers, match the fold pattern observed in outcrop (cf. Fig. 1b).

Most of the pyrrhotite are standalone grains in the 3D visuals, whereas some pyrite grains are intergrown or touching each other (Figs. 2a and 3e). In horizontal and E-W striking vertical gray slices (Figs. 3a,f) as well as the 3D rendered images (Figs. 3c,e), pyrrhotite grains mimic the bulk finite strain ellipsoid with their long (X) and short (Z) axes being aligned E-W and N-S, respectively. Turning the core (~90°) and looking west, the pyrrhotite grains appear flattened or oblate in the Y-Z plane (Figs. 3i,j; see also 7f).

3.3. Segmentation of pyrrhotite and pyrite

Segmentation of pyrrhotite and pyrite grains was performed with ImageJ and in-house written software as follows. In order to reduce imaging noise, the reconstructed tomographic image was filtered with variance weighted mean filter (noise variance = 500, radius = 2 pixels; Gonzalez and Woods, 2002). After filtering, contrast to noise ratio between mineral crystals and background was high (>~8), and thus the crystals could be segmented using simple thresholding. The threshold value was determined using Tsai's moment preserving thresholding method (Tsai, 1985). After thresholding, the image contained pyrrhotite and pyrite grains as white regions, and additionally some small white regions caused by imaging noise that is typically found in tomographic images and caused by various processes such camera noise and variance in the count of X-ray photons received by the camera (Stock, 2008). Regions corresponding to imaging noise were suppressed by removing all white regions whose volume was less than 20 voxels, a cut-off that seemed to remove noise regions efficiently but preserve even the smallest crystals. Finally, pyrite and pyrrhotite grains were separated manually based on the characteristic cubic or parallelepipedic shape of pyrite.

Pyrrhotite grains were separated from each other using watershed segmentation (Meyer and Beucher, 1990) seeded with local maxima of distance map. In order to avoid over-segmentation near locations with multiple nearby local maxima, only the largest of them was taken to be a seed point. The resulting segmentation was checked by visually comparing the segmented regions to the original data. The quality of the segmentation was found to be satisfactory. Each segmented grain or crystal was analyzed separately. Grain volumes were calculated as the number of voxels in the grain. The orientations of long (X), intermediate (Y) and short (Z) axes were determined by counting voxels along three mutually perpendicular principal axes within the grain (Pearson, 1901). The aspect ratio was determined as the ratio between the lengths of the X and the Z axes, and the Flinn parameters were calculated as ratios between the X and Y, and Y and Z, respectively.

Finally, the orientation data for all grains were plotted in rose diagrams for the horizontal plane and for vertical planes (Figs. 4a,b and 5a,b). Pyrite grains were separated from each other and analyzed similarly as pyrrhotite grains, but applying a closing operation with radius of 5 pixels before watershed segmentation. A flowchart summarizing the image processing operations is shown in Appendix 1, and provided as an electronic supplement.

3.4. 3D quantitative analysis

We collected quantitative data for volume, surface area, aspect ratio (X/Z and Y/Z), and orientation of pyrrhotite and pyrite grains. The volume fraction in the whole rock sample obtained through full segmentation of pyrite and pyrrhotite is 3.5±0.3% and 4±2%, respectively, where the uncertainty estimates have been made according to Fusseis et al., (2012). A total of 25,920 pyrrhotite and 155 pyrite grains were encountered but grains touching the edges or boundary of the sample were discarded due to incomplete size and axes attributes.

Pyrrhotite X-axes plunge shallowly (~ 22°) towards the east, whereas metasedimentary layers (S0) dips about 45° in the same direction (Figs. 3c-f and 4a,b). The mean aspect ratio and volume of the pyrrhotite grains are ~14 and 0.019 mm^3, respectively (Figs. 4c,e). A small fraction of pyrrhotite grain (about 4%) have a much higher aspect ratio as others reaching a maximum value of 292 (Fig. 4c). The Flinn diagram portrays dominantly prolate shapes of pyrrhotite grains, although with a significant fraction of oblate shapes (Fig. 4d). We interpret the latter as representing pyrrhotite microboudins (see micro-textural description below). Aspect ratio increases with increasing grain volume (Fig. 4e).

The horizontal rose diagram for the long axes of pyrite grains (Fig. 5a) shows a wide range of trends with a main E-W maximum and weaker N-S maximum (Fig. 5a) that can be correlated with L^1_2 and L^0_1, respectively. The rose diagram of Fig. 5b shows that the long axes (X) of pyrite grains generally pitch shallowly in both EW and N-S vertical sections. The 3D images show that the larger pyrite grains are confined to a single layer located in the middle of the sample (Figs. 3c,e). The mean aspect ratio of pyrite grains is about 4 with a smaller spread as observed for pyrrhotite grains. The Flinn diagram for pyrite grains indicates a mixture of highly prolate to highly oblate shapes (Fig. 5d), whereas the volume to aspect ratio plot reveals a slightly inverse relationship between grain volume and aspect ratio (Fig. 5e). We now proceed to compare the above described 3D data for the shape and orientation of the two main sulfide minerals in the studied sample with AMS fabrics and microstructural observations in thin section.

4. Anisotropy of magnetic susceptibility (AMS) analyses

4.1. Pyrrhotite, AMS and tectonic fabric

Pyrrhotite (density 4.6 g/cm^3) is a magnetically ordered (ferromagnetic) mineral that, at ambient temperature, has its atomic magnetic moments arranged at the lattice scale (e.g., Borradaile and Jackson, 2010). Because of this magneto-crystalline property, a correlation between the AMS and rock deformation fabrics has been proposed as a proxy for 3D strain geometry (e.g., Parsons et al., 2016). The shape of the AMS ellipsoid has been shown to be a function of the deformation history in a rock and the response of minerals to deformation in terms of deformation mechanisms (e.g., Borradaile and Jackson, 2004).

AMS is defined by a symmetric second rank tensor (Nye, 1957) that gives the ratio (K = M/H) between an applied magnetic field (M) and the induced magnetization (H) in different directions. The principal axes of the AMS ellipsoid or principal susceptibility axes, K1, K2, and K3, define the magnetic foliation (K1-K2 plane), and magnetic lineation (K1; Tarling and Hrouda, 1993). The mean susceptibility (Km) is the average of K1, K2 and K3 (Janák, 1965). The corrected degree of anisotropy (P') is a measure of the deviation of the AMS ellipsoid ($P'>1$) from a perfect sphere ($P'=1$). The shape of the AMS ellipsoid can be defined as prolate ($T= -1$, $K1 > K2 = K3$) or oblate ($T = 1$, $K1 = K2 > K3$) end members depending on the strain conditions and mineral behavior (e.g., Borradaile and Jackson, 2004).

It has been shown that AMS is mainly controlled by ferromagnetic and paramagnetic minerals in a rock, whereas diamagnetic minerals have only a minimal effect (e.g., Borradaile and Jackson, 2010; Ferré et al., 2014). Strong SPO and LPO of ferromagnetic minerals produce a magnetic foliation and lineation that reflect the bulk rock fabric. The principal susceptibility axes (K1, K2, K3) may or may not correspond to finite strain axes ($X \geq Y \geq Z$), and depending on crystallographic properties and deformation mechanism, an inverse or blended relationship can result other than the expected strain axes (Rochette et al., 1999; Ferré, 2002; Borradaile et al., 2012).

To identify the origin of AMS in a given rock sample, both ferromagnetic and paramagnetic minerals can be decoupled by measuring and plotting their thermomagnetic or susceptibility-temperature (K/T) curves and Curie points (Hrouda et al., 1997). The thermomagnetic curves represent the variation with temperature (heating and cooling effects) of magnetic susceptibility (Hrouda, 1994) and can be used to constrain the mineral species that are the magnetic carriers in a sample (e.g. Skyttä et al., 2010; Karell et al., 2014). A detailed account on the AMS and petrofrabrics of deformed and metamorphosed rocks can be found in seminal reviews by Borradaile and Jackson, (2004, 2010).

4.2. Analytical methods

For this study, AMS and temperature variation of the magnetic susceptibility (K/T) experiments were performed at the Research Laboratory, Geological Survey of Finland in Espoo. The 2.5 cm × 8 cm (diameter × length) drill core (sample 57) that was partly used for the μ-CT analysis was cut into three pieces of 2.1 cm length each. AMS was analyzed with a KLY-3S Kappabridge, operating at a frequency of 875 Hz and with a field intensity of 300 Am^{-1}, while rotating each subsample about three mutually perpendicular axes to construct its magnetic susceptibility axes and determine the corresponding magnetic parameters. Thermomagnetic measurements were performed using CS-3 furnace apparatus (Agico, Inc.). The AMS and thermomagnetic data were processed with the Anisoft (version 4.2) and Cureval (version 8) programs, respectively.

4.3. AMS results

The mean magnetic susceptibility (Km) of the 3 subsamples has a high value ranging from 17703 to 23308 μSI, whereas the corrected degree of anisotropy (P') varies from 1.81 to 1.94 (Fig. 6). The shape of the AMS ellipsoid (T) is clearly prolate with T values of -0.14 to -0.23. The thermomagnetic curve shows a typical pattern of pyrrhotite with an abrupt drop in magnetization at ~325°C (Hrouda et al., 1997), suggesting that AMS is mainly controlled by this mineral. The orientation of the magnetic foliation matches that of the east-west striking and subvertically dipping S2 foliation (Fig. 6d; cf. Fig. 1b), whereas the short axis (K3) is oriented perpendicular to this plane. The orientation of the triaxial magnetic ellipsoid also coincides with the principal X, Y and Z axes of pyrrhotite determined through the µ-CT (cf. Figs. 3 and 4).

5. Petrographic and SEM analyses

Three thin sections were cut from the sample normal and parallel to the main S2 matrix foliation and L^1_2 intersection lineation. The horizontal thin section shows a penetrative, highly differentiated and finely-spaced S2 foliation striking east-west (Fig. 7a). The long axes (X) of most pyrrhotite grains are well aligned with this fabric (Fig. 7b). Pyrite grains are wrapped by S2 suggesting pre- or syn-D2 growth (Zwart, 1962; Passchier and Trouw, 2005). No inclusions of pyrrhotite were found inside pyrite, at least in these three thin sections. Some pyrrhotite grains appear microboudinaged in east-west direction (Fig. 7c) with the boudin necks filled with silicate minerals. As mentioned earlier, oblate pyrrhotite grains in the Flinn diagram of Fig. 4d probably represent microboudins of originally larger prolate grain, or alternatively, grains weakly deformed during D2 and retaining their original (syn-D1) oblate shape (Figs. 7e,f).

The vertical N-S section cut normal to S2 and the mineral stretching lineation reveals a high-angle relationship between S2 overprinting S1 (Figs. 7d-f) and a stage 4 crenulation cleavage morphology in the scheme of Bell and Rubenach (1983). An important observation in this section is that the Y-axes of pyrrhotite grains are parallel to S1 but truncated, deflected or even folded by S2 (Figs. 7e,f) indicating that this mineral grew prior to D2. Close examination of pyrrhotite grains reveals variable shapes ranging from flattened parallel to S1, to oval shaped parallel to S2, to microfolded with axial planes parallel to S2 (Fig. 7f). Pyrrhotite grains with Y- and Z-axes parallel and perpendicular to the S1 foliation, respectively, are relatively less deformed. Whereas, highly deformed pyrrhotite grains have Y- and Z-axes perpendicular and parallel to the S1 in the same thin section.

The section cut parallel to S2 (Fig. 8) shows the finely laminated layers already seen in the µ-CT images (Fig. 3), wherein pyrrhotite grains plunge shallowly (25°) towards the east (Fig. 8d). Pyrite grains have euhedral outlines and are associated with symmetric fibrous quartz strain fringes more or less aligned E-W with the stretching lineation and L^1_2 intersection lineation.

In order to verify the chemical composition of sulfides, Energy-dispersive X-ray Spectroscopy (EDS) analyses were performed at the Research Laboratory, Geological Survey of Finland in Espoo, using an Oxford Instruments EDS-spectrometer X-Max 80 mm^2 (SDD) attached to a JEOL JSM 7100F Schottky field emission scanning electron microscope (representative FE-SEM images and EDS spectra are provided in Appendix 2 as an electronic supplement). The analytical conditions were as follows: high vacuum mode, a COMPO back-scattered signal (BSE), 20 kV accelerating voltage and 0.5 nA probe current. FE-SEM and EDS analyses showed that almost all pyrite grains are partially to completely pseudomorphed by pyrrhotite (Fig. 9), indicating prograde heating resulting in sulphur release from pyrite (Craig and Vokes, 1993). Skeletal textures mark this pyrrhotite to pyrite replacement (Fig. 9b). Besides, we detected inclusions of euhedral arsenopyrite and anhedral sphalerite around the median and rim regions of pseudomorphed pyrite (Figs. 9a,b). EDS analyses, conducted in an FE-SEM, of both intact and microboudinaged grains confirmed their pyrrhotite composition (Figs. 9c,d). Some of the cubic-looking grains have rhombic shape possibly due to replacement of diagenetic anhydrite by pyrrhotite (Hall, 1982).

6. Discussion

6.1. Implications for the D1 related structures

Microstructures commonly exhibit complex overprinting relationships that are only partially reflected by outcrop-scale structures (Aerden, 1998; Sayab et al., 2016b). This counts in particular for Proterozoic belts, where glacially eroded bedrock and sedimentary cover exacerbate field observations in the 3rd dimension. Under such limited exposure conditions, oriented drill cores are useful to understand multiple fabric overprinting relationships and microstructures (Sayab, et al., 2015). As described earlier, sample 57 was extracted from a D2 low-strain zone of a flat-lying folded surface, where the east-west striking pervasive fabric marks the axial planar S2 foliation. High-resolution tomographic 3D images accompanied by a vertical east-west oriented thin section revealed that metasedimentary layers (S0) dips ~23° more steeply than the S1 foliation, whereas the intersection lineation (L^0_1) is north-south trending and shallowly plunging (Fig. 10). This structural relationship suggests that the sample comes from the normal limb of an F1 recumbent fold, in which deformation was partitioned between top-to-the west shearing components and perpendicular shortening components (Fig. 10), consistent with the east-vergent D1 thrusting and folding event of Lahtinen et al. (2015).

The secondary north-south preferred orientation seen in the rose diagram of Fig. 5a suggests that pyrite porphyroblasts were aligned N-S during D1. During D2 they would have developed their main E-W preferred orientation (Figs. 5a and 11), probably associated with pressure solution as that is the dominant deformation mechanism of pyrite in greenschist facies conditions (McClay and Ellis, 1983) (Fig. 5b). Pyrrhotite X-axes do not retain a primitive N-S direction, which is expected because as a much weaker mineral, it would have experienced much stronger deformation during D2 as pyrite (cf. Craig and Vokes, 1993).

The shape and spatial distribution of pyrite and pyrrhotite grains could also be influenced by the preferential growth in S1 microlithons or low-strain lenses, given the control of deformation partitioning on metamorphic reactions in general (Bell and Hayward, 1991). Additionally, the growth of sulfide minerals was concentrated in alternate metasedimentary layers, probably because of a chemically more favorable composition (Figs. 3c,d,e).

Microtextural relationships show that arsenopyrite and sphalerite are cogenetic with pyrite, whereas the latter was partially to completely replaced by pyrrhotite. Thermodynamic modelling of the arsenopyrite-sphalerite-pyrite and pyrrhotite assemblage in closed-system metapelites (e.g., Lynch and Mengel, 1995) indicate upper-greenschist facies conditions at intermediate pressures of 5.5-6.9 kbars, and these P-T estimates can potentially be applied to D1 in the study area.

6.2. Implications for the D2 structures

The north-south oriented vertical thin section, cut perpendicular to S2 and normal to L^1_2 reveals a high-angle relationship between S1 and S2 (Figs. 7e,f). We already showed that pyrrhotite and pyrite porphyroblasts formed syn-D1 because pyrrhotite grains are aligned parallel to S1, but truncated and deformed by S2 (Fig. 7f), whereas pyrite grains are wrapped by S2 and developed syn-D2 strain fringes. We, therefore, infer two possible tectonic scenarios: 1) that the K3 axes of the AMS ellipsoid (pyrrhotite porphyroblasts) changed from subvertical (normal to a thrusting-related S1) to gently south-dipping normal to S2. In other words, the K2 and K3 axes interchanged positions during D2, while K1 was maintained constant (Figs. 11a,b), 2) alternatively, the K1, K2 and K3 axes all interchanged positions during D2, similar to the pyrite porphyroblasts where all three principal axes of the shape ellipsoid switched from D1 to D2 (Figs. 5a and 11). Thus, the SPO of pyrrhotite during D1 depends on the geometry of the AMS axes (Fig. 11b).

We have argued that the magnetic foliation reflects an originally north-south striking and shallowly east dipping orientation of S1 and of axial planes of F1 recumbent folds (Figs. 10 and 11b). We further propose that progressive bulk inhomogenous shortening associated with foliation development (Bell and Rubenach, 1983) controlled the growth, orientation and AMS properties of pyrrhotite and pyrite porphyroblasts (Fig. 11a). Both minerals grew during D1 in low-strain microlithons bounded by S1 cleavage planes as manifested by the preferred orientation of pyrrhotite parallel to S1. With the development of S2, porphyroblast growth ceased and symmetric strain fringes grew off pyrite grains parallel to the E-W maximum extension direction.

Aeromagnetic image and field observations around the Martimo area show a type-2 fold interference pattern, where the east-west striking upright F2 folds deform east-vergent, shallowly dipping F1 folds locally resulting in crescent-mushroom or arrowhead surface patterns (Fig. 1a). The general fold pattern is characterized by a major synform in the south and antiform in the north (Lahtinen et al., 2015). This regional scale geometry fits well with our interpretation of fabrics in the studied sample, which comes from the core of the synformal D2 structure (cf. Figs. 1a, 10 and 11c). A more extensive description of the deformation sequence can be found in Lahtinen et al. (2015). Our integrated approach and workflow of combining µ-CT, AMS and microstructures can be highly useful and applied to unfold the complex structural history, especially for the mineralized bedrock such as the Peräpohja region.

6.3. Complementary character of AMS and µ-CT techniques

µ-CT quantitative data provide 3D information for metamorphic textures that significantly complements and allow a more rigorous interpretation of AMS results. More specifically, µ-CT data add statistical mineral abundances, spatial distribution, size and shape of different mineral species with a precision that cannot be achieved with other methods. In the case that concerns us here, the magnetic lineation (K1) was shown to coincide with the X-axis of pyrrhotite grain volumes (cf. Figs. 4a,b and 6d), whereas a Flinn plot for these grains shows predominant prolate shapes in agreement with the AMS shape parameter (T) and anisotropy (P'). In addition, our µ-CT data reveal that both pyrrhotite and pyrite grains are localized along alternating metasedimentary layers suggesting that the sulfide growth was chemically controlled by individual laminae, and were formed during D1 to form metamorphic porphyroblasts. The study of thin sections is still indispensable for revealing microstructural relationships between deformation fabrics and different minerals, as shown herein for pyrite and pyrrhotite grains with respect to S1 and S2 foliations, the truncation, shape and micro-folding of pyrrhotite by S2, or the microboudinage textures.

7. Conclusions

a. By adding the 3D shape and preferred orientations of sulfide and magnetic minerals in a rock, µ-CT can significantly enhance the interpretation of bulk rock AMS, particularly in multiply deformed rocks. In addition, integrating µ-CT and AMS methods are highly useful in interpreting metamorphic textures in 3D.

b. In this study, we have shown that the AMS principal susceptibility axes experienced major changes between two successive deformation phases associated with a horizontal (S1) and subvertical (S2) foliations. K3 changed its orientation from normal to S1 to normal to S2 foliations, while K1 was maintained. Alternatively, the long axes of both pyrite and pyrrhotite porphyroblasts changed from N-S to E-W orientations during D1 and D2, respectively. The sample scale interpretations fit well with the regional scale type-2 fold interference pattern.

c. Quantitative measurements of individual pyrrhotite grains demonstrate a predominance of highly prolate shapes, whereas pyrite grains have more equant geometry reflecting the higher strength of this less-deformed mineral. Our µ-CT images highlighted the localization of sulfide minerals along alternating metasedimentary layers that crystallized as porphyroblasts during the D1 metamorphism.

d. 3D petrography using multiple oriented thin sections was crucial for unravelling the deformation history of the studied sample. We conclude that conventional thin section microstructural analysis cannot be substituted, but only complemented by more sophisticated techniques such as µ-CT and AMS.

Acknowledgements

We thank R. Lahtinen, F. Molnar and S. Mertanen for useful discussions, M. Lehtonen for help with the FE-SEM imaging, A. Kallonen for acquiring and reconstructing the X-ray computed tomography data at the Helsinki University, and P. Telkkälä for help with the mini drill in the field. We acknowledge A. Käpyaho for initiating the research collaboration between the GTK and Jyväskylä University. Constructive journal reviews were made by Eric C. Ferré and Florian Fusseis. We are thankful to Toru Takeshita for his editorial handling and useful suggestions.

Supplementary data

Appendix 1 and 2 are provided as an electronic supplement.

References

Aerden, D., 2003. Preferred orientation of Planar microstructures determined via statistical best-fit of measured intersection-lines: The “FitPitch” computer program. Journal of Structural Geology 25, 923–934. https://doi.org/10.1016/S0191-8141(02)00119-0

Aerden, D.G.A.M., 1998. Tectonic evolution of the Montagne Noire and a possible orogenic model for syncollisional exhumation of deep rocks, Variscan belt, France. Tectonics 17, 62–79. https://doi.org/10.1029/97TC02342

Bell, T.H., Bruce, M.D., 2006. The internal inclusion trail geometries preserved within a first phase of porphyroblast growth. Journal of Structural Geology 28, 236–252. https://doi.org/10.1016/j.jsg.2005.11.001

Bell, T.H., Hayward, N., 1991. Episodic metamorphic reactions during orogenesis: the control of deformation partitioning on reaction sites and reaction duration. Journal of Metamorphic Geology 9, 619–640. https://doi.org/10.1111/j.1525-1314.1991.tb00552.x

Bell, T.H., Rubenach, M.J., 1983. Sequential porphyroblast growth and crenulation cleavage development during progressive deformation. Tectonophysics 92, 171–194. https://doi.org/10.1016/0040-1951(83)90089-6

Bell, T.H., Rubenach, M.J., 1980. Crenulation cleavage development—evidence for progressive bulk inhomogeneous shortening from “millipede” microstructures in the robertson river metamorphics. Tectonophysics 68, T9–T15. https://doi.org/10.1016/0040-1951(80)90003-7

Borradaile, G.J., Almqvist, B.S.G., Geneviciene, I., 2012. Anisotropy of magnetic susceptibility (AMS) and diamagnetic fabrics in the Durness Limestone, NW Scotland. Journal of Structural Geology 34, 54–60. https://doi.org/10.1016/j.jsg.2011.10.008

Borradaile, G.J., Jackson, M., 2010. Structural geology, petrofabrics and magnetic fabrics (AMS, AARM, AIRM). Journal of Structural Geology 32, 1519–1551. https://doi.org/10.1016/j.jsg.2009.09.006

Borradaile, G.J., Jackson, M., 2004. Anisotropy of magnetic susceptibility (AMS): magnetic petrofabrics of deformed rocks. Geological Society, London, Special Publications 238, 299–360. https://doi.org/10.1144/GSL.SP.2004.238.01.18

Craig, J.R., Vokes, F.M., 1993. The Metamorphism of Pyrite and Pyritic Ores: An Overview. Mineralogical Magazine 57, 3–18. https://doi.org/10.1180/minmag.1993.057.386.02

Ferré, E.C., 2002. Theoretical models of intermediate and inverse AMS fabrics. Geophysical Research Letters 29, 29–32. https://doi.org/10.1029/2001GL014367

Ferré, E.C., Gébelin, A., Till, J.L., Sassier, C., Burmeister, K.C., 2014. Deformation and magnetic fabrics in ductile shear zones: A review. Tectonophysics 629, 179–188. https://doi.org/10.1016/j.tecto.2014.04.008

Fusseis, F., Schrank, C., Liu, J., Karrech, A., Llana-Funez, S., Xiao, X., Regenauer-Lieb, K., 2012. Pore formation during dehydration of a polycrystalline gypsum sample observed and quantified in a time-series synchrotron X-ray micro-tomography experiment. Solid Earth 3, 71–86. https://doi.org/10.5194/se-3-71-2012

Gonzalez, R., Woods, R., 2002. Digital image processing, Prentice Hall. https://doi.org/10.1016/0734-189X(90)90171-Q

Hall, A.J., 1982. Gypsum as a precursor to pyrrhotite in metamorphic rocks - Evidence from the Ballachulish State, Scotland. Mineralium Deposita 17, 401–409.

https://doi.org/10.1007/BF00204468

Hanna, R.D., Ketcham, R.A., 2017. X-ray computed tomography of planetary materials: A primer and review of recent studies. Chemie Der Erde - Geochemistry 1–26. https://doi.org/10.1016/j.chemer.2017.01.006

Hayward, N., 1990. Determination of early fold axis orientations in multiply deformed rocks using porphyroblast inclusion trails. Tectonophysics 179, 353–369. https://doi.org/10.1016/0040-1951(90)90301-N

Hrouda, F., 1994. A technique for the measurement of thermal changes of magnetic susceptibility of weakly magnetic rocks by the CS-2 apparatus and KLY-2 Kappabridge. Geophysical Journal International 118, 604–612. https://doi.org/10.1111/j.1365-246X.1994.tb03987.x

Hrouda, F., Jelínek, V., Zapletal, K., Jelinek, V., Zapletal, K., Jelínek, V., 1997. Refined technique for susceptibility resolution into ferromagnetic and paramagnetic components based on susceptibility temperature-variation measurement. Geophysical Journal International 129, 715–719. https://doi.org/10.1111/j.1365-246X.1997.tb04506.x

Janák, F., 1965. Determination of anisotropy of magnetic susceptibility of rocks. Studia Geophysica et Geodaetica 9, 290–301.

Karell, F., Ehlers, C., Airo, M.L., 2014. Emplacement and magnetic fabrics of rapakivi granite intrusions within Wiborg and Aland rapakivi granite batholiths in Finland. Tectonophysics 614, 31–43. https://doi.org/10.1016/j.tecto.2013.12.006

Kruckenberg, S.C., Ferré, E.C., Teyssier, C., Vanderhaeghe, O., Whitney, D.L., Seaton, N.C.A., Skord, J.A., 2010. Viscoplastic flow in migmatites deduced from fabric anisotropy: An example from the Naxos dome, Greece. Journal of Geophysical Research: Solid Earth 115, 1–18. https://doi.org/10.1029/2009JB007012

Kyle, J.R., Ketcham, R.A., 2015. Application of high resolution X-ray computed tomography to mineral deposit origin, evaluation, and processing. Ore Geology Reviews 65, 821–839. https://doi.org/10.1016/j.oregeorev.2014.09.034

Lahtinen, R., Sayab, M., Karell, F., 2015. Near-orthogonal deformation successions in the polydeformed Paleoproterozoic Martimo belt: Implications for the tectonic evolution of Northern Fennoscandia. Precambrian Research 270, 22–38.

Macente, A., Fusseis, F., Menegon, L., Xianghui, X., John, T., 2017. The strain-dependent spatial evolution of garnet in a high-P ductile shear zone from the Western Gneiss Region (Norway): a synchrotron X-ray microtomography study. Journal of Metamorphic Geology 35, 565–583. https://doi.org/10.1111/jmg.12245

McClay, K.R., Ellis, P.G., 1983. Deformation and Recrystallization of Pyrite. Mineralogical Magazine 47, 527–538. https://doi.org/10.1180/minmag.1983.047.345.14

Meyer, F., Beucher, S., 1990. Morphological segmentation. Journal of Visual Communication and Image Representation. https://doi.org/10.1016/1047-3203(90)90014-M

Nykänen, V., Niiranen, T., Molnár, F., Lahti, I., Korhonen, K., Cook, N., Skyttä, P., 2017. Optimizing a Knowledge-driven Prospectivity Model for Gold Deposits Within Peräpohja Belt, Northern Finland. Natural Resources Research. https://doi.org/10.1007/s11053-016-9321-4

Parsons, A.J., Ferre, E.C., Law, R.D., Lloyd, G.E., Phillips, R.J., Searle, M.P., 2016. Orogen-parallel deformation of the Himalayan midcrust: Insights from structural and magnetic fabric analyses of the Greater Himalayan Sequence, Annapurna-Dhaulagiri Himalaya, central Nepal. Tectonics 35, 2515–2537. https://doi.org/10.1002/2016TC004244

Passchier, C.W., Trouw, R.A.J., 2005. Microtectonics, Springer-Verlag Berlin Heidelberg.

Pearson, K., 1901. On lines and planes of closest fit to systems of points in space. The London, Edinburgh, and Dublin Philosophical Magazine and Journal of Science. https://doi.org/10.1080/14786440109462720

Ranta, J.-P., Hanski, E., Cook, N., Lahaye, Y., 2016. Source of boron in the Palokas gold deposit, northern Finland: evidence from boron isotopes and major element composition of tourmaline. Mineralium Deposita. https://doi.org/10.1007/s00126-016-0700-x

Ranta, J.-P., Lauri, L.S., Hanski, E., Huhma, H., Lahaye, Y., Vanhanen, E., 2015. U–Pb and Sm–Nd isotopic constraints on the evolution of the Paleoproterozoic Peräpohja Belt, northern Finland. Precambrian Research 266, 246–259.

https://doi.org/http://dx.doi.org/10.1016/j.precamres.2015.05.018

Riller, U., Cruden, A.R., Schwerdtner, W.M., 1996. Magnetic fabric and microstructural evidence for a tectono-thermal overprint of the early Proterozoic Murray pluton, central Ontario, Canada. Journal of Structural Geology 18, 1005–1016. https://doi.org/10.1016/0191-8141(96)00028-4

Rochette, P., Aubourg, C., Perrin, M., 1999. Is this magnetic fabric normal? A review and case studies in volcanic formations. Tectonophysics 307, 219–234. https://doi.org/10.1016/S0040-1951(99)00127-4

Sayab, M., Shah, S.Z., Aerden, D., 2016b. Metamorphic record of the NW Himalayan orogeny between the Indian plate-Kohistan Ladakh Arc and Asia: Revelations from foliation intersection axis (FIA) controlled P-T-t-d paths. Tectonophysics 671, 110–126.

Sayab, M., Suuronen, J.P., Hölttä, P., Aerden, D., Lahtinen, R., Kallonen, A.P., 2015. High-resolution X-ray computed microtomography: A holistic approach to metamorphic fabric analyses. Geology 43, 55–58.

Sayab, M., Suuronen, J.P., Molnár, F., Villanova, J., Kallonen, A., O'Brien, H., Lahtinen, R., Lehtonen, M., 2016a. Three-dimensional textural and quantitative analyses of orogenic gold at the nanoscale. Geology 44, 739–742. https://doi.org/10.1130/G38074.1

Skyttä, P., Hermansson, T., Elming, S.Å., Bauer, T., 2010. Magnetic fabrics as constraints on the kinematic history of a pre-tectonic granitoid intrusion, Kristineberg, northern Sweden. Journal of Structural Geology 32, 1125–1136. https://doi.org/10.1016/j.jsg.2010.06.020

Stock, S., 2008. Microcomputed Tomography: Methodology and Applications. CRC Press. https://doi.org/CAT# 58762

Tarling, D.H., Hrouda, F., 1993. The Magnetic Anisotropy of Rocks. Chapman and Hall, London. https://doi.org/10.1002/gj.3350300111

Tsai, W.-H., 1985. Moment-preserving thresolding: A new approach. Computer Vision, Graphics, and Image Processing. https://doi.org/10.1016/0734-189X(85)90133-1

Figure Captions

Fig. 1. (a) Aeromagnetic map of the study area showing the location of sample 57. The area shows distinct mushroom-shape or arrowhead patterns typical of type-2 fold interference. A main antiform and synform pair can be distinguished. Inset on the top left shows a schematic 3D model. (b) Field photograph and line diagram of S0/S1 overprinted by S2, and drill core location.

Fig. 2. Three-dimensional microstructures of sample 57 based on X-ray computed microtomography (μ-CT). The drill core is oriented and digitally chopped at three different levels to show the penetrative pyrrhotite fabric. Images on the left (a,c,e and g) are 3D side views, whereas those on the right (b,d,f, and h) are horizontal top-view slices. S denotes south. Pyrrhotite (po) and pyrite (py) are rendered yellow except for (b).

Fig. 3. Different 2D and 3D representations of μ-CT data. (a) Horizontal 2D grayscale slice showing east-west aligned (X-axis) pyrrhotite (po) grains. (b) Volume rendering of the same image as shown in (a). (c,d,e) Side views, looking to the north and perpendicular to the long axes (X) of the pyrrhotite grains. Prolate pyrrhotite grains and cubic pyrite (py) are localized in alternating mm-scale metasedimentary layers (S0). The latter dips 45° east, whereas pyrrhotite long axes plunge more shallowly (~22°) in the same direction. (f) Grayscale μ-CT slice showing textural characteristics of pyrrhotite, pyrite and S0 and S1 relationship. (g) Folded metasedimentary layers are segmented (isolated) in red and blue. (h) Top 3D view of the drill core showing pyrrhotite grains in the X-Z axes. (i) 3D rendered side view along the Y-Z plane. (j) The same Y-Z plane is shown as a grayscale μ-CT slice. Pyrrhotite and pyrite are rendered yellow in (b), (c), (e), (g), (h) and (i).

Fig. 4. Quantitative geometric analyses of pyrrhotite grains. (a) Rose plot showing the preferred east-west alignment of pyrrhotite long axes (X). (b) Plunge values of X-axes of pyrrhotite averaging 22°. (c) Aspect ratio plot with a mean ratio of about 14. (d) Flinn diagram showing the tendency of grains towards the prolate shape, with a minor population of oblate shape (see text for discussion). (e) Aspect ratio vs. grain volume plot showing a trend between logarithms of grain volume and aspect ratio, where volume increases with increase in the aspect ratio.

Fig. 5. Quantitative geometric analysis of pyrite grains. (a) Rose diagram for the long axes (X) of pyrite grains showing large spread with an E-W maximum, and a weaker N-S maximum. (b) Plunges of pyrite long axes are predominantly shallow (20-30°). (c) Aspect ratio diagram with an average value of about 4. (d) Flinn diagram for pyrite showing highly variable shapes of this mineral, but much lower aspect ratios than the pyrrhotite. (e) Aspect ratio vs. grain volume plot showing a minor volume increase with decreasing aspect ratio.

Fig. 6. (a) Mean susceptibility (Km) vs. anisotropy degree (P′) plot showing typical values of pyrrhotite. (b) Shape parameter (T) vs. anisotropy degree (P') suggesting prolate shapes of pyrrhotite grains. (c) Heating (red) and cooling (blue) thermomagnetic curves showing a drop at about 325 °C, typical of pyrrhotite. (d) AMS plot showing east-west striking magnetic foliation (K1-K2) and shallowly plunging magnetic lineation (K1) carried by pyrrhotite.

Fig. 7. Oriented photomicrographs showing microtextures in sample 57. (a) Horizontal thin section showing S2 deflecting around a pyrite (py) porphyroblast, crossed polarized light. Inset shows the μ-CT image marking the actual section plane. (b-c) Close ups from the horizontal thin section in (a) showing (b) intact, and (c) microboudinaged pyrrhotite (po) porphyroblasts elongated along S2, reflected light photomicrographs. (d) N-S vertical thin section showing change in the shape of pyrrhotite porphyroblasts from oblate to prolate. Strain fringes developed on the upper and lower faces of the pyrite porphyroblasts could be a cut effect (cf. Fig. 8b), crossed polarized light. (e) Close-up of the same thin section as ‘d’, showing pyrrhotite porphyroblasts truncated, deflected or microfolded by S2, plane polarized light. (f) Photomicrograph, plane polarized light image digitally rendered to

enhance the shape of pyrrhotite grains using image-processing tools, and associated sketch showing microstructures associated with the deformation of the pyrrhotite grains (N-S vertical section). The SPO of the pyrrhotite changes from oblate to prolate controlled by S1 and S2, respectively.

Fig. 8. (a) E-W vertical thin section and (b) sketch showing face-controlled syn-D2 strain fringes developed on the eastern and western faces of pyrite, crossed polarized light image. (c) Micro-CT image corresponding to the actual E-W vertical section shown in (a). (d-e) Close-ups of (a) showing (d) pyrrhotite (po) plunging towards the east, and (e) strain fringes developed on the edge of the pyrite porphyroblasts. Both close-ups are taken under the crossed polarized light.

Fig. 9. FE-SEM images of sample 57. Red dots are EDS spots (see Appendix 2). (a) Pyrite totally replaced by pyrrhotite. The rim contains two unaltered sphalerite grains. (b) Pyrite-pyrrhotite replacement front associated with transitional skeletal texture. Euhedral arsenopyrite inclusions were not replaced by the pyrrhotite. (c) Single pyrrhotite grain plunging towards the east in an E-W vertical section (half arrow points up and East). (d) Pyrrhotite microboudinaged in the E-W direction (cf. Fig. 7c).

Fig. 10. Interpreted large-scale tectonic context of the sample in the normal limb of an F1 recumbent fold based on S0-S1 relationships in the sample.

Fig. 11. (a) Conceptual model showing progressive bulk inhomogeneous shortening during D2 causing steepening of S1 and pyrrhotite grains. Change in the SPO of both pyrite (py) and pyrrhotite (po) is controlled by the S2. (b) Two possible D1-related SPO geometries are presented: 1) prolate, and 2) oblate. In the former case, K1 retained the original orientation from D1 to D2. In the latter case, K1 changed orientation from N-S (D1) to E-W (D2). In either case, the S1 is striking N-S and shallowly dipping towards the east, consistent with the orientation obtained from the μ-CT image (cf. Fig. 10). (c) Present day geometrical configuration forming type-2 fold interference pattern.

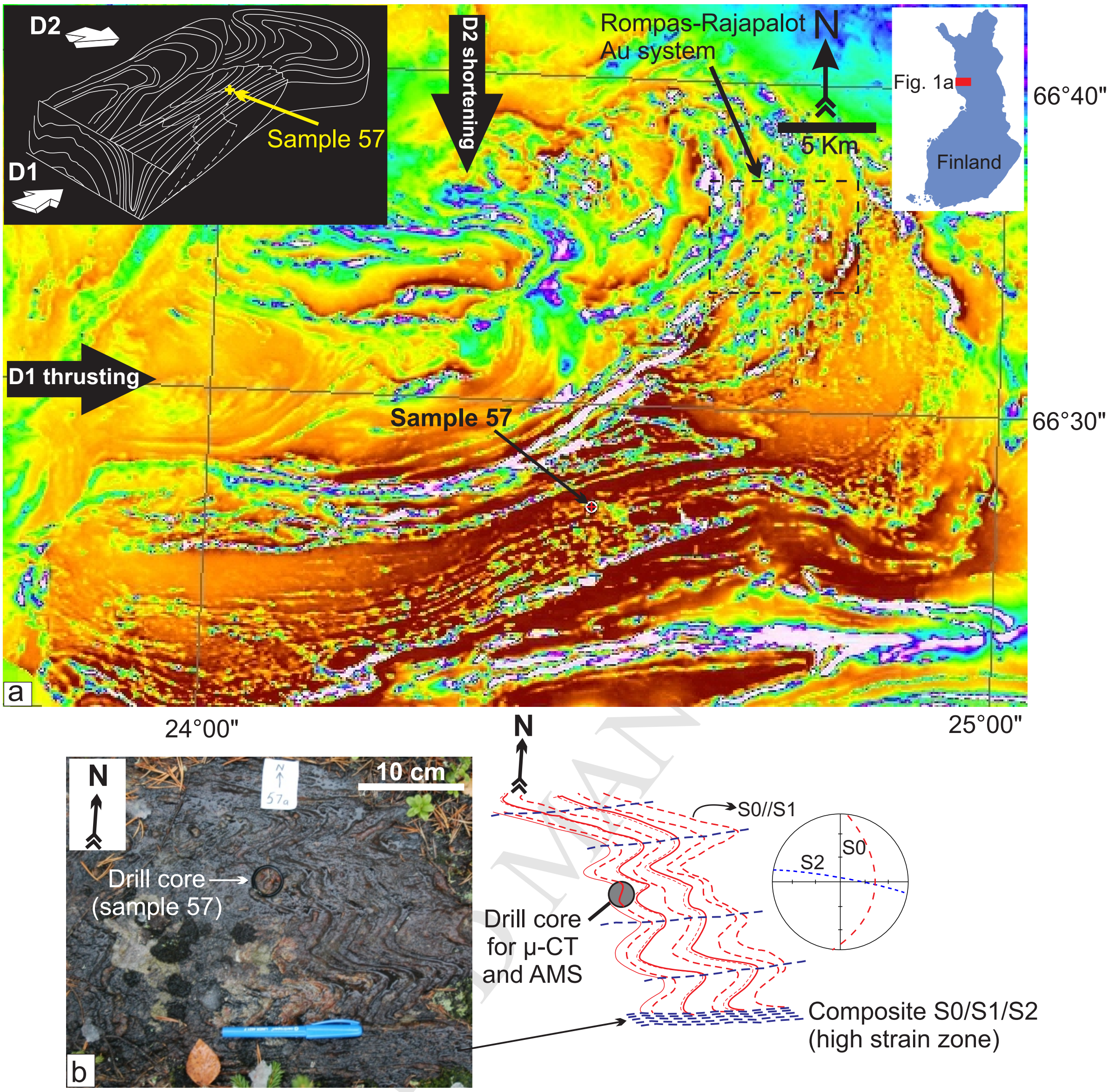
D2
Sample 57
D1
D2 shortening
Rompas-Rajapalot
Au system
N
5 Km
Fig. 1a
Finland
66°40"
D1 thrusting
Sample 57
66°30"
a
24°00"
25°00"
N
10 cm
Drill core
(sample 57)
b
N
S0//S1
S0
S2
Drill core
for µ-CT
and AMS
Composite S0/S1/S2
(high strain zone)

Fig. 1

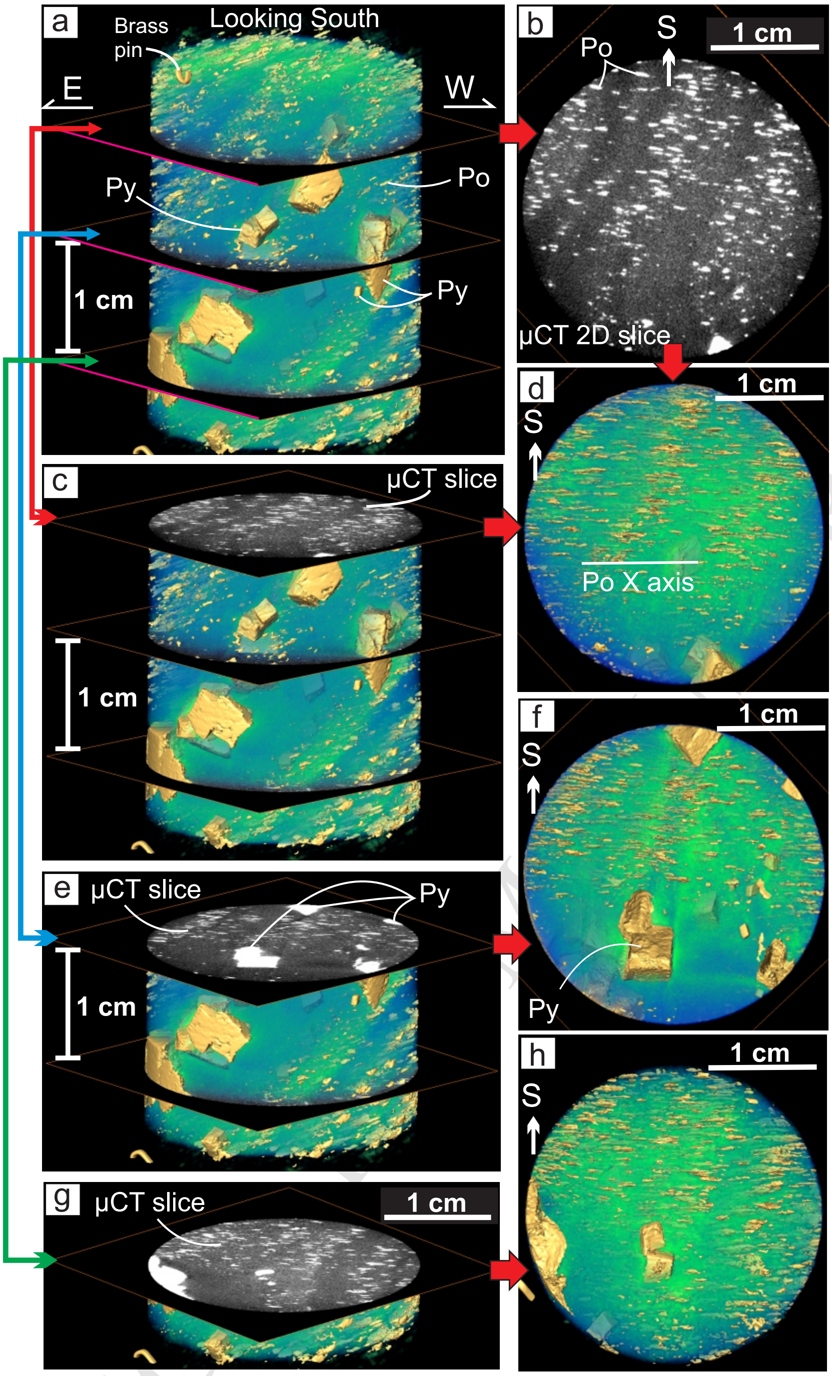
a
Brass pin
Looking South
E
W
Py
Po
Py
1 cm
b
Po
S
1 cm
µCT 2D slice
c
µCT slice
1 cm
d
S
1 cm
Po X axis
e
µCT slice
Py
1 cm
f
S
1 cm
Py
g
µCT slice
1 cm
h
S
1 cm

Fig. 2

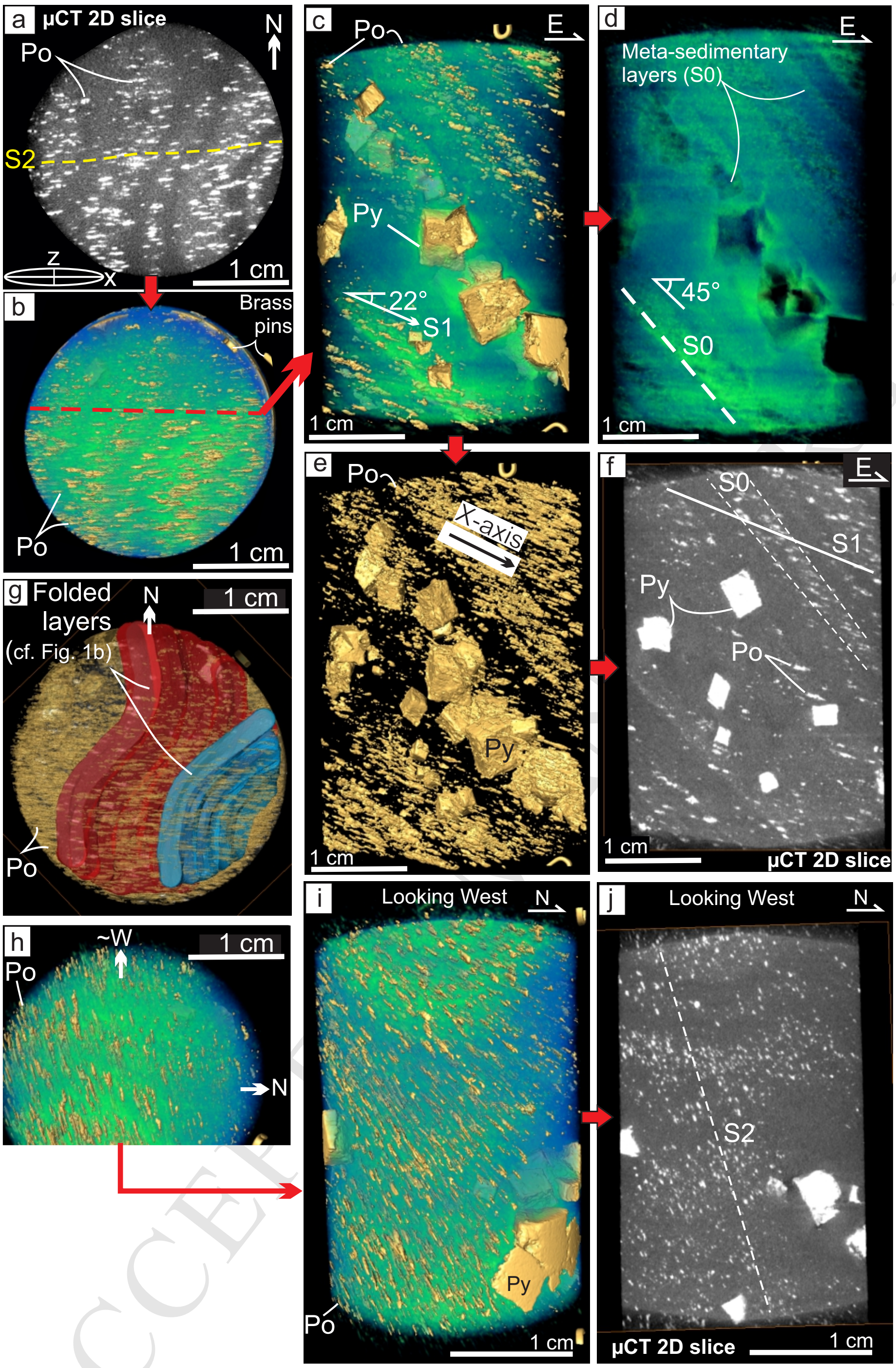
a
µCT 2D slice
N
Po
S2
Z
X
1 cm
b
Brass
pins
Po
1 cm
c
Po
E
Py
22°
S1
1 cm
d
E
Meta-sedimentary
layers (S0)
45°
S0
1 cm
e
Po
X-axis
Py
1 cm
f
S0
E
S1
Py
Po
1 cm
µCT 2D slice
g
Folded
layers
(cf. Fig. 1b)
N
1 cm
Po
h
~W
1 cm
Po
N
i
Looking West
N
Py
Po
1 cm
j
Looking West
N
S2
µCT 2D slice
1 cm

Fig. 3

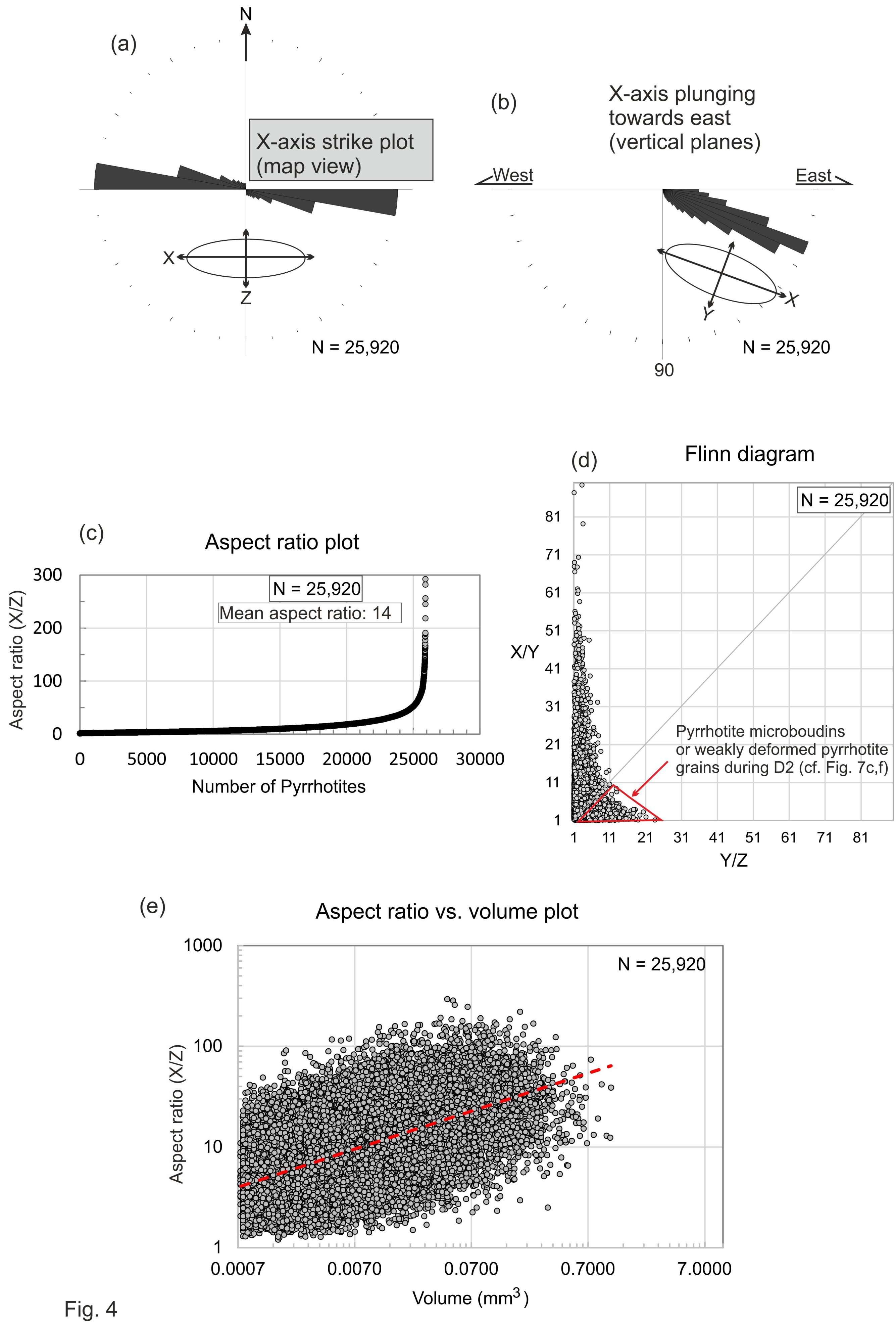

(a)
N
X-axis strike plot
(map view)
X
Z
N = 25,920
(b)
X-axis plunging
towards east
(vertical planes)
West
East
Y
X
90
N = 25,920
(c)
Aspect ratio plot
N = 25,920
Mean aspect ratio: 14
Aspect ratio (X/Z)
300
200
100
0
0
5000
10000
15000
20000
25000
30000
Number of Pyrrhotites
(d)
Flinn diagram
N = 25,920
X/Y
81
71
61
51
41
31
21
11
1
1
11
21
31
41
51
61
71
81
Y/Z
Pyrrhotite microboudins
or weakly deformed pyrrhotite
grains during D2 (cf. Fig. 7c,f)
(e)
Aspect ratio vs. volume plot
N = 25,920
Aspect ratio (X/Z)
1000
100
10
1
0.0007
0.0070
0.0700
0.7000
7.0000
Volume (mm3)

Fig. 4

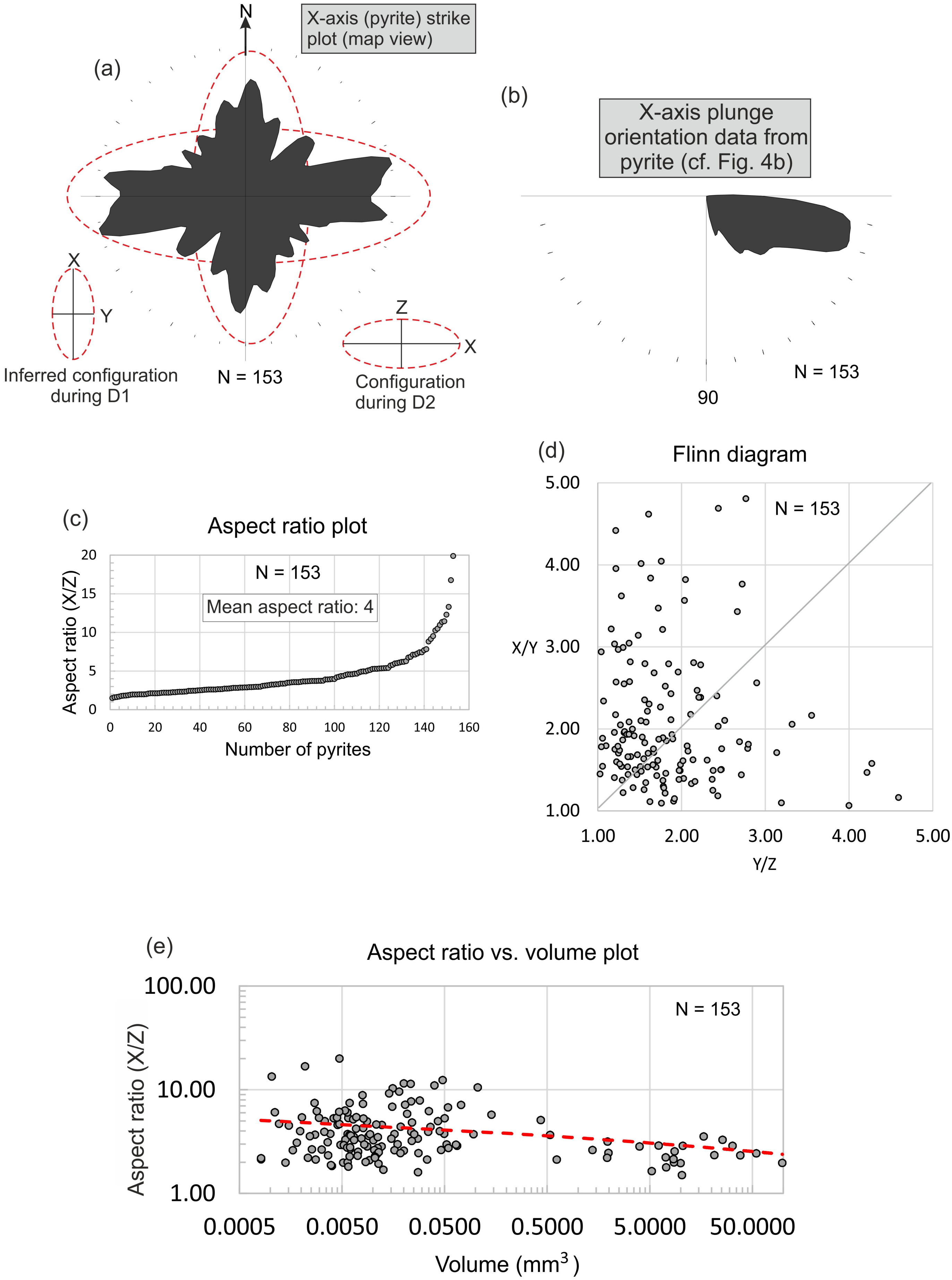

N
X-axis (pyrite) strike plot (map view)
(a)
X
Y
Inferred configuration during D1
N = 153
Z
X
Configuration during D2
(b)
X-axis plunge orientation data from pyrite (cf. Fig. 4b)
N = 153
90
(c)
Aspect ratio plot
N = 153
Mean aspect ratio: 4
Aspect ratio (X/Z)
20
15
10
5
0
0
20
40
60
80
100
120
140
160
Number of pyrites
(d)
Flinn diagram
5.00
4.00
X/Y 3.00
2.00
1.00
N = 153
1.00
2.00
3.00
4.00
5.00
Y/Z
(e)
Aspect ratio vs. volume plot
100.00
10.00
1.00
Aspect ratio (X/Z)
N = 153
0.0005
0.0050
0.0500
0.5000
5.0000
50.0000
Volume (mm3)

Fig. 5

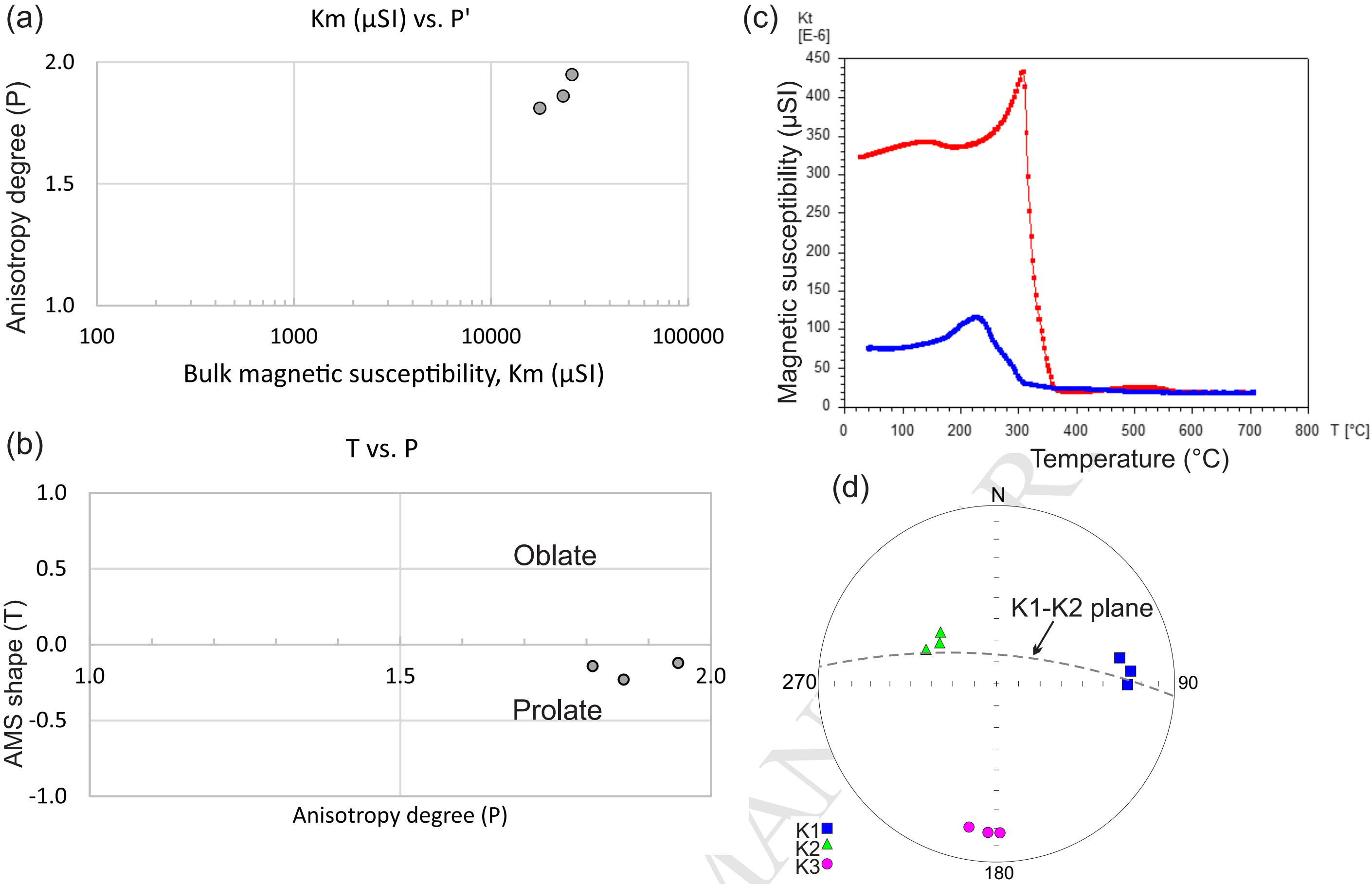
(a)
Km (µSI) vs. P'
Anisotropy degree (P)
2.0
1.5
1.0
100
1000
10000
100000
Bulk magnetic susceptibility, Km (µSI)
(b)
T vs. P
AMS shape (T)
1.0
0.5
0.0
-0.5
-1.0
1.0
1.5
2.0
Oblate
Prolate
Anisotropy degree (P)
(c)
Kt
[E-6]
Magnetic susceptibility (µSI)
450
400
350
300
250
200
150
100
50
0
0
100
200
300
400
500
600
700
800
T [°C]
Temperature (°C)
(d)
N
K1-K2 plane
270
90
180
K1
K2
K3

Fig. 6

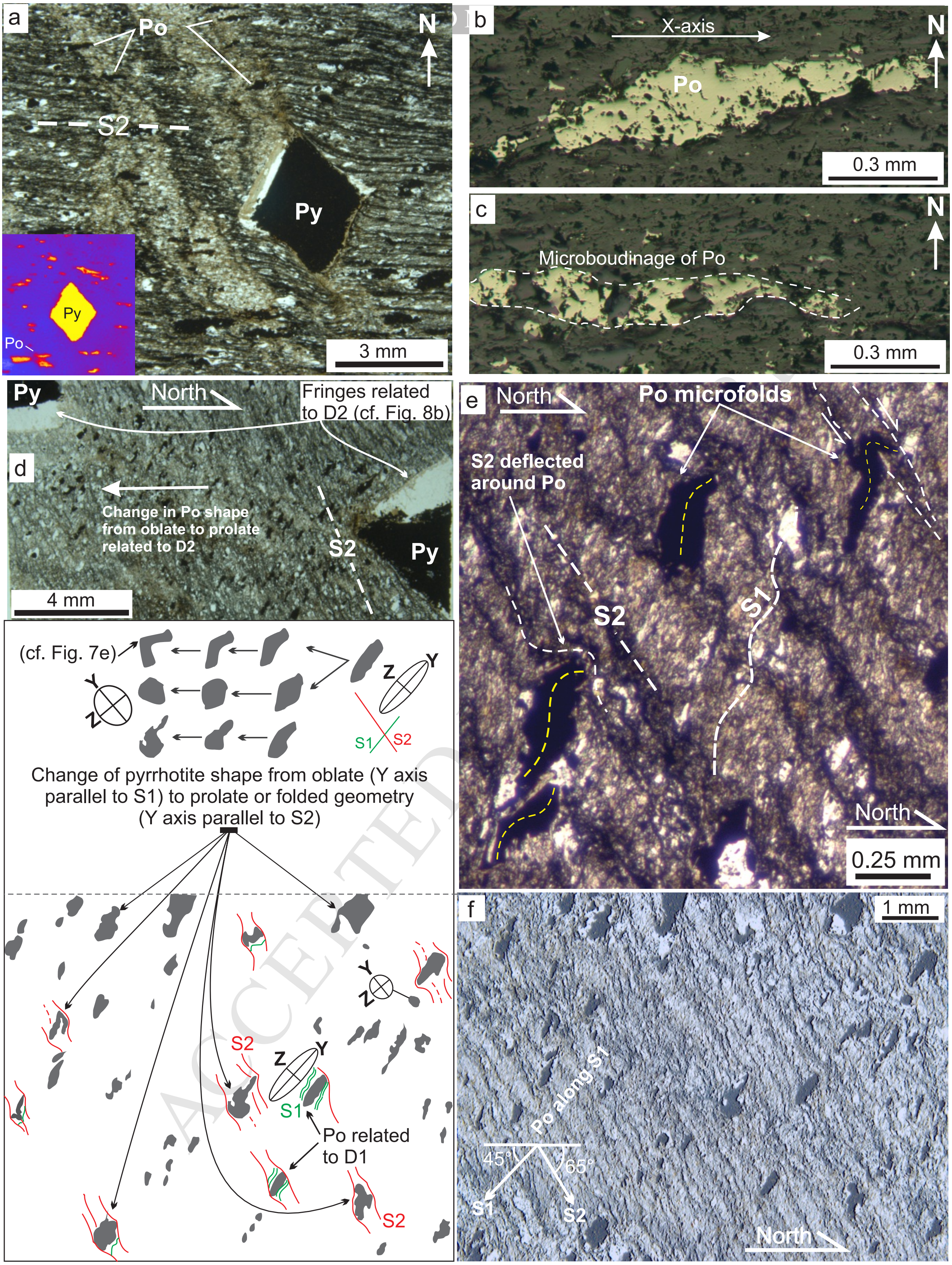

a
Po
S2
Py
Py
Po
3 mm
N
b
X-axis
Po
0.3 mm
N
c
Microboudinage of Po
0.3 mm
N
Py
North
Fringes related to D2 (cf. Fig. 8b)
d
Change in Po shape from oblate to prolate related to D2
S2
Py
4 mm
e
North
Po microfolds
S2 deflected around Po
S2
S1
North
0.25 mm
(cf. Fig. 7e)
Z
Y
S1
S2
Change of pyrrhotite shape from oblate (Y axis parallel to S1) to prolate or folded geometry (Y axis parallel to S2)
S2
Z
Y
S1
Po related to D1
S2
f
1 mm
Po along S1
45°
65°
S1
S2
North

Fig. 7

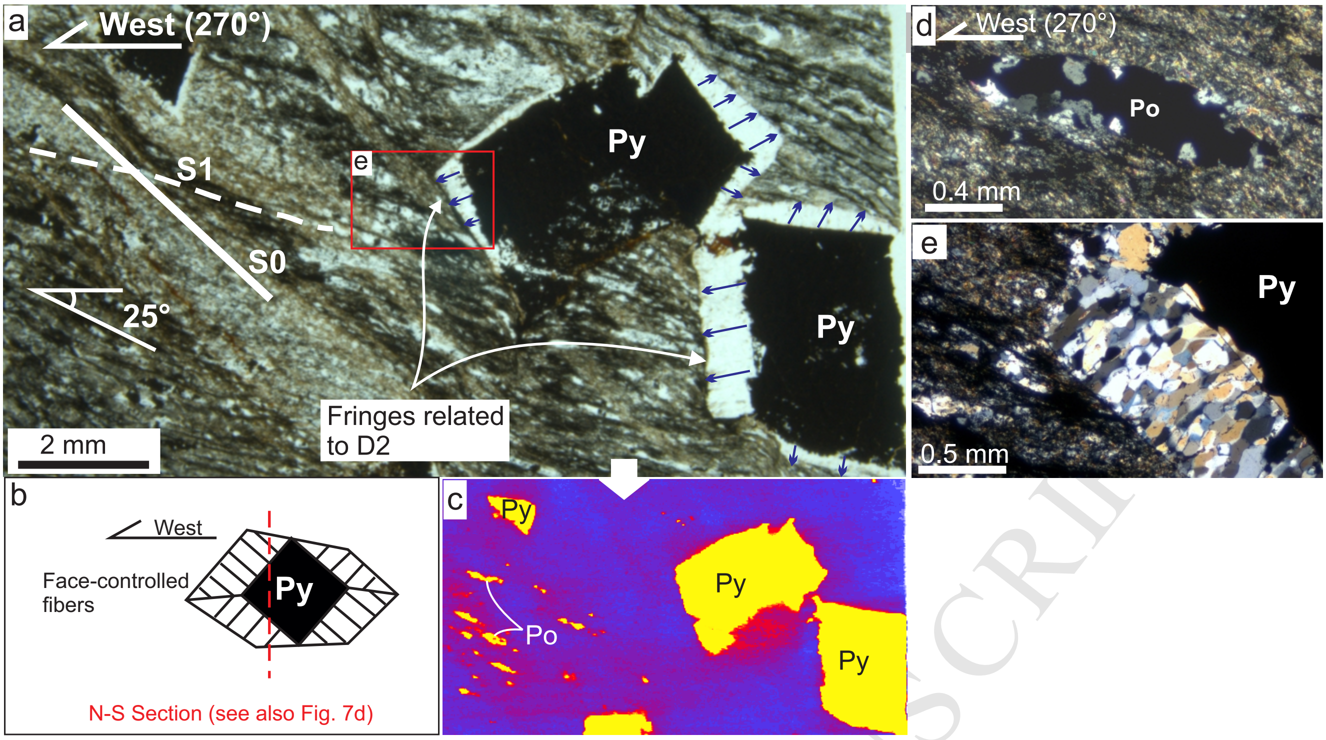

a
West (270°)
S1
S0
25°
e
Py
Py
Fringes related to D2
2 mm
d
West (270°)
Po
0.4 mm
e
Py
0.5 mm
b
West
Face-controlled fibers
Py
N-S Section (see also Fig. 7d)
c
Py
Po
Py
Py

Fig. 8

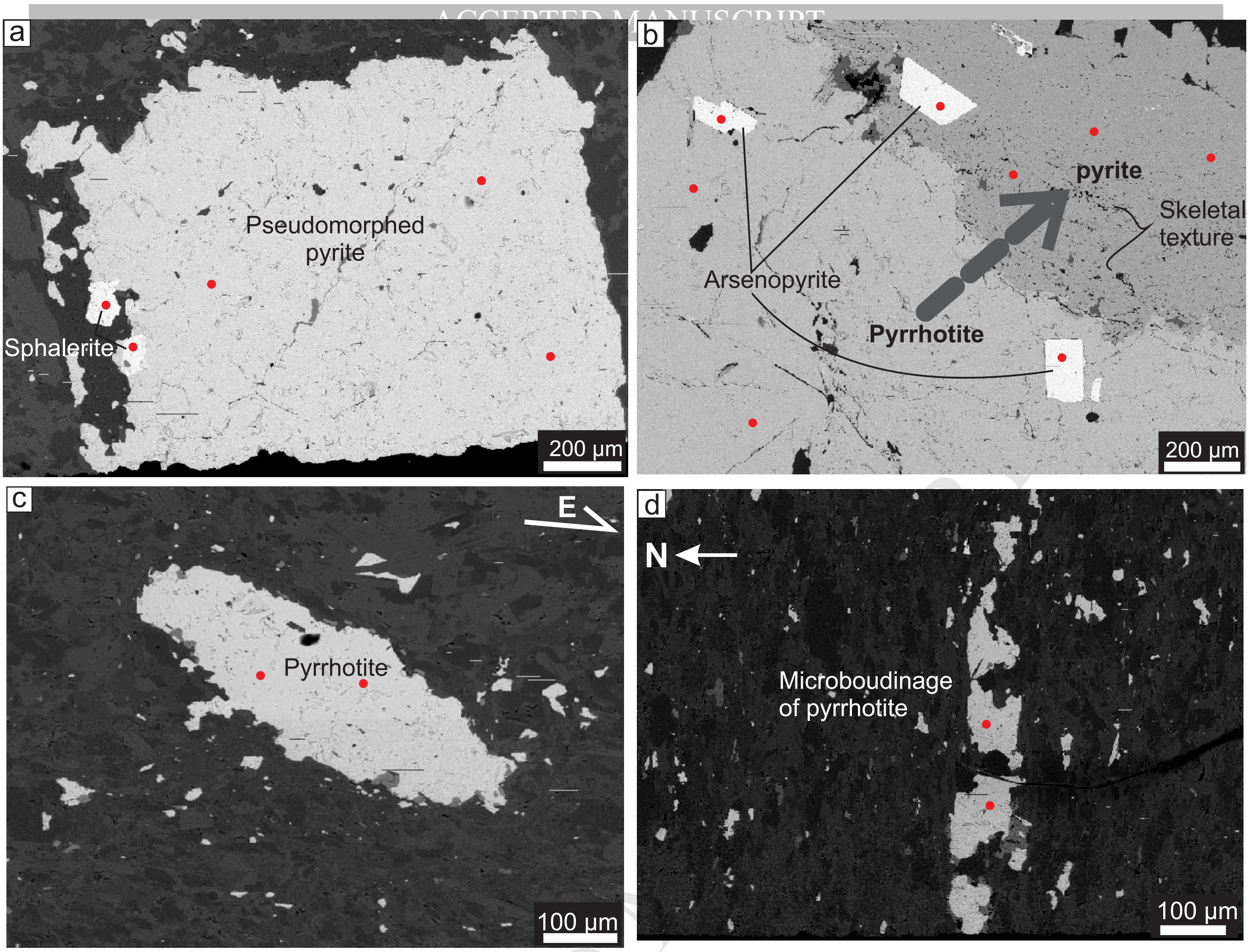
a
Pseudomorphed pyrite
Sphalerite
200 µm
b
pyrite
Skeletal texture
Arsenopyrite
Pyrrhotite
200 µm
c
E
Pyrrhotite
100 µm
d
N
Microboudinage of pyrrhotite
100 µm

Fig. 9

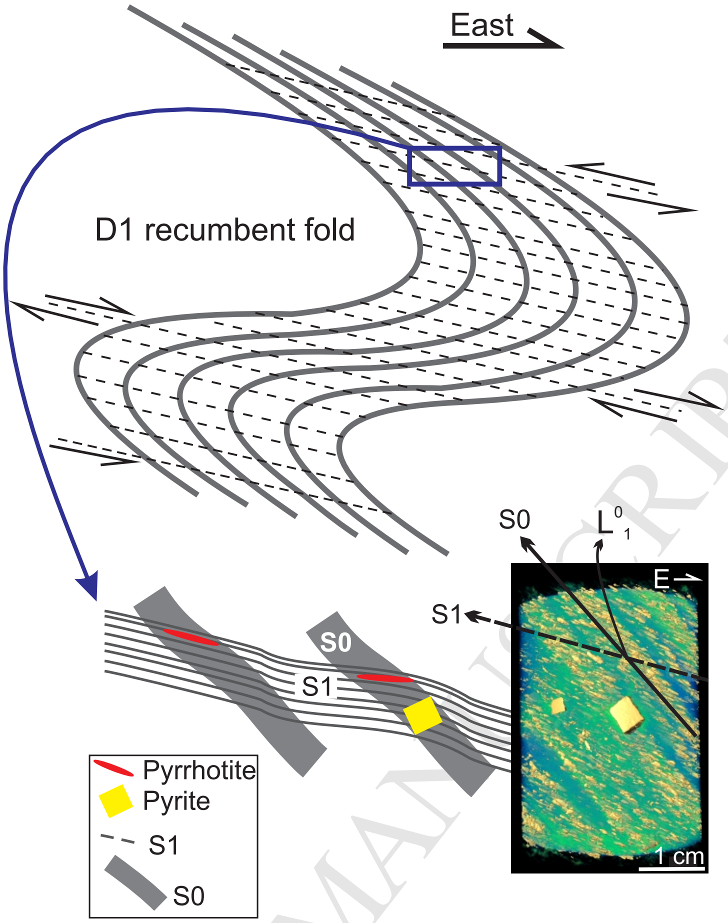
East
D1 recumbent fold
S0
L^0_1
E
S1
S0
S1
1 cm
Pyrrhotite
Pyrite
S1
S0

Fig. 10

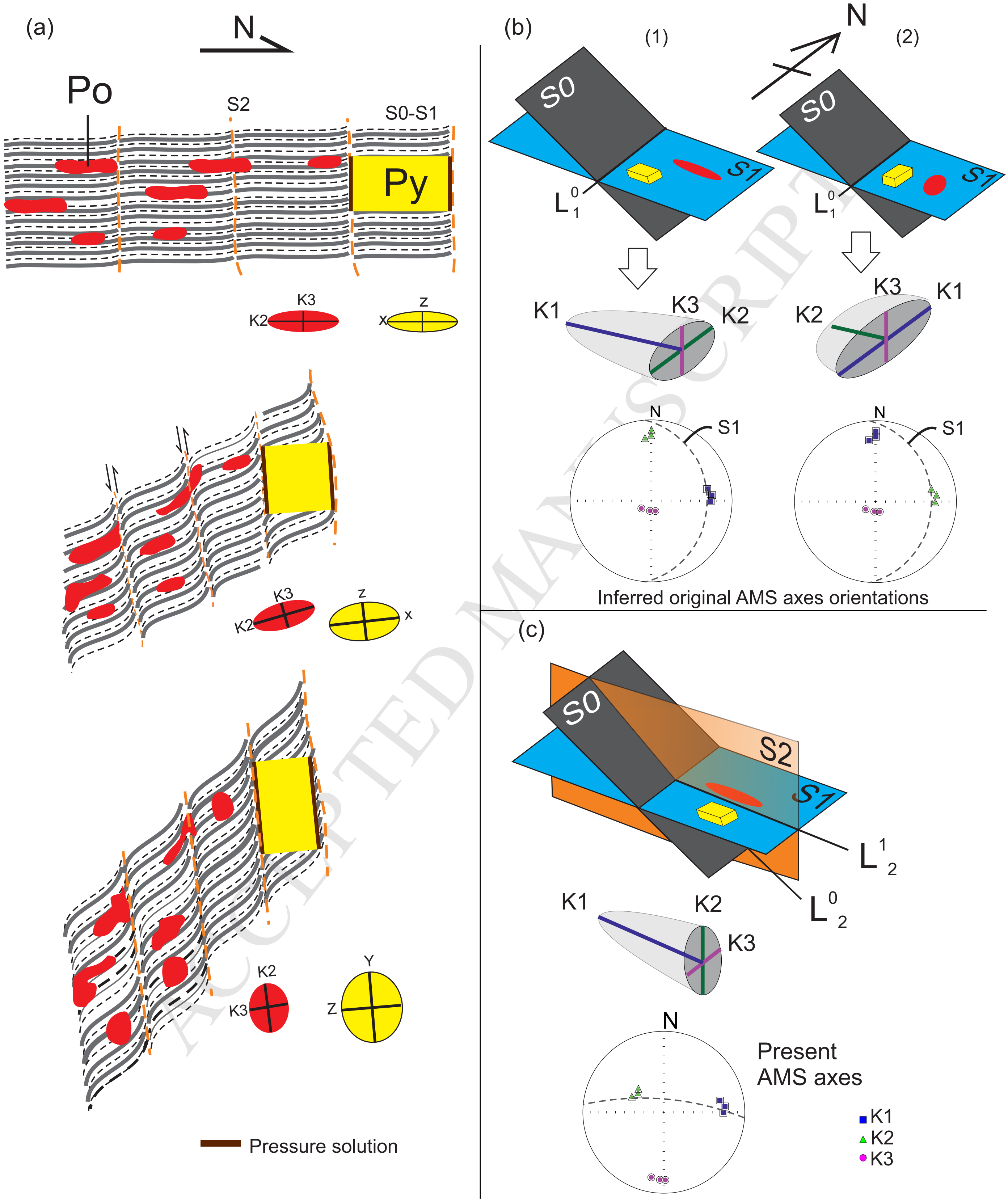

(a)
N
Po
S2
S0-S1
Py
K3
K2
Z
X
K3
K2
Z
X
K2
K3
Y
Z
Pressure solution
(b)
(1)
(2)
N
S0
S1
L_1^0
K1
K3
K2
N
S1
Inferred original AMS axes orientations
(c)
S0
S2
S1
L_2^1
L_2^0
K1
K2
K3
N
Present
AMS axes
K1
K2
K3

Fig. 11

Highlights

Bulk rock AMS is integrated with the X-ray computed µ-tomography and 3D petrography

Change in the SPO is seen, wherein AMS ellipsoid axes were switched from D1 to D2

Type-2 fold interference is deduced based on AMS and two near-orthogonal foliations